# Robust perpendicular magnetization of Co nanomagnets against alloy composition

Hung-Hsiang Yang,[1,2,*] Chuan-Che Hsu,[3] Wen-Chin Lin,[3] and Yukio Hasegawa[1]
[1]*Institute for Solid State Physics, the University of Tokyo, 5-1-5, Kashiwa-no-ha, Kashiwa, Chiba 277-8581, Japan*
[2]*Physical Institute, Karlsruhe Institute of Technology, 76131 Karlsruhe, Germany*
[3]*Department of Physics, National Taiwan Normal University, Taipei, 116, Taiwan*

(Received 8 February 2021; revised 2 July 2021; accepted 6 July 2021; published 19 July 2021)

$Co_{1-x}Fe_x$ bilayer nanomagnets formed on a Cu(111) substrate with the alloy composition of $x = 0$, 0.2, 0.5, 0.8, and 1 were investigated using scanning tunneling microscopy (STM). The islands with $x = 0$, 0.2, and 0.5 were further studied using spin-polarized STM. With $x = 0.2$, the nanoislands exhibit triangular shapes similar to the pure Co islands with an upward shift in the peak energy of the minority $d$ state. On the other hand, at $x = 0.5$, the appearance of the nanoislands evolve to a round shape, and the peak energy is distributed irregularly within the islands. A hexagonal shape and inhomogeneous electronic states similar to pure Fe islands are observed on the $x = 0.8$ islands. The magnetic field dependence of the spin-sensitive signal revealed that the perpendicular anisotropy of the $Co_{1-x}Fe_x$ alloy islands is persistent up to half of the Fe alloy composition.

DOI: 10.1103/PhysRevB.104.035422

## I. INTRODUCTION

Fe, Co, and Ni are the most commonly used elements for magnetic thin-film engineering in the research field of spintronics [1–16]. These magnetic 3$d$ transition metals prefer the different primary crystalline structure of body-centered cubic (bcc), hexagonal close-packed (hcp), and face-centered cubic (fcc) structures, respectively. Therefore, when epitaxially grown on a heterogeneous substrate, the magnetic properties such as magnetic anisotropy may change by the lattice distortion and the subsequent strain relaxation through the modifications in magnetocrystalline, magnetoelastic, and magnetic shape anisotropies [5–10]. Varying the film thickness may also lead to structural transformations [1,2] and spin-reorientation transition [3,4] through the competition among the various magnetic anisotropies. The energy of magnetic shape anisotropy is directly related with the magnitude of the magnetic moment [17]. According to the Slater-Pauling curve [18], the averaged magnetic moments of the 3$d$ transition metal alloys are determined by the number of the valence electrons per atom. The preferred magnetization direction with respects to the crystal lattice, on the other hand, is determined by the magnetocrystalline anisotropy. In the case of 3$d$ magnets, the magnetocrystalline anisotropy is derived from the second-order perturbation of the spin-orbit interaction [17]. Accordingly, the preferred magnetization orientations are closely related to its electronic states near the Fermi level, i.e., valence $d$-orbital occupation. In the alloyed systems, the electron occupation of each element is affected significantly by the presence of the hetero components [19,20]. Thereby, tailoring alloy composition of thin films enables us to control the magnetic properties, as demonstrated with binary-alloy thin films of the 3$d$ transition metals [20–22]. In the case of $Co_{1-x}Fe_x$ alloy thin films formed on Cu(100), increasing the Fe composition results in the reduction of the number of 3$d$ electrons, i.e., hole doping, which is expected from fewer number of $d$ electrons in Fe than Co. A subtle change in the averaged band filling occasionally leads to drastic changes in the energy of magnetic anisotropy, as reported in previous literatures [19–22].

In the submonolayer regime, nanosized magnetic islands emerge. In contrast to the continuous thin films of mm-$\mu$m lateral size, nanosized two-dimensional islands are more applicable in the future nanoscale spintronic devices. The reduction in lateral size ($\sim$10 nm) and vertical thickness [1–2 monolayer (ML)] gives rise to exotic quantum confinement effects such as surface state interferences [23]. Magnetic nanoislands have been widely studied using spin-polarized scanning tunneling microscopy (SP-STM) and spectroscopy [24–43]. One of the most studied samples is submonolayer Co/Cu(111) [25–30], which exhibits triangular islands with a height of two atomic layers on the Cu substrate. Depending on the stacking configuration at the interface, two distinct orientations of the islands were found. Perpendicular magnetic anisotropy of the Co islands has been identified using SP-STM [28–30]. In the case of Fe bilayer islands on Cu(111), the first layer of Fe follows the same crystalline structure of the Cu(111) substrate (pseudomorphic). The second layer is mostly pseudomorphic except for the corners of the islands, in which the atomic arrangement is relaxed to form bcc stacking [35]. More researches on the properties of magnetic nanoislands have been reported, e.g., Fe/Cu(111) [31–35], Fe/Au(111) [36–39], Co/Ag(111) [40], and Co/Au(111) [41–43]. However, microscopic magnetic properties of alloy magnetic nanoisland remains unexplored.

In this paper, we report on our investigation of the morphological, electronic, and magnetic properties of $Co_{1-x}Fe_x$ alloy nanomagnets ($x = 0$, 0.2, 0.5, 0.8, and 1) using spin-averaged and spin-polarized STM (magnetic properties are investigated for the islands with $x = 0$, 0.2, and 0.5). Two-ML-high $Co_{1-x}Fe_x$ nanosized island with the alloy

*hung-hsiang.yang@kit.edu

 

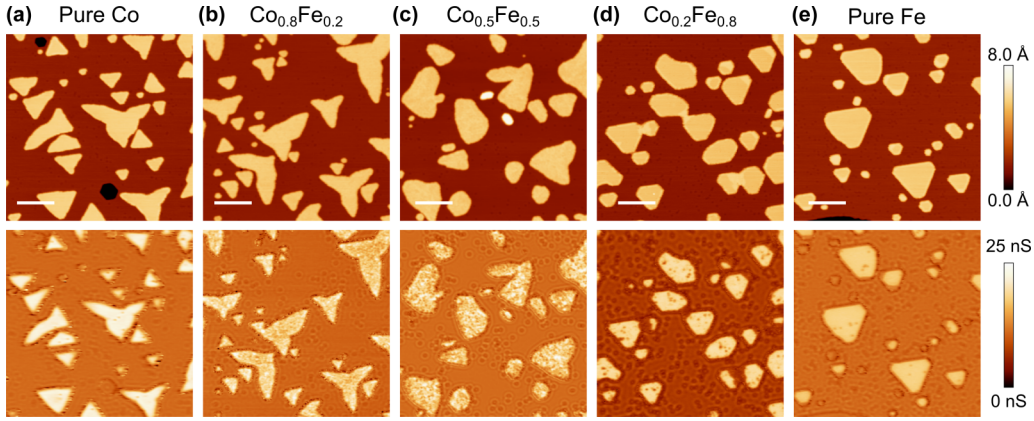


FIG. 1. Typical STM images and the corresponding $dI/dV$ images of (a) Co, (b) $Co_{0.8}Fe_{0.2}$, (c) $Co_{0.5}Fe_{0.5}$, (d) $Co_{0.2}Fe_{0.8}$, and (e) Fe islands on Cu(111). The scale bars drawn in the STM images correspond to 20 nm. Measurement conditions: sample bias voltage ($V_s$): [(a)–(c) and (e)] −300 mV and (d) −350 mV, tunneling current ($I_t$) = 1 nA, and modulation voltage ($V_{\text{mod}}^{\text{PP}}$) = 50 mV.

concentration of $x = 0$, 0.2, 0.5, 0.8, and 1 were successfully grown on Cu(111) surface using molecular beam epitaxy. The STM images revealed similar triangular islands for $x = 0$ and 0.2, while for $x = 0.5$ distinct round-shaped islands appear. The Fe-rich islands with $x = 0.8$, and 1 show similar hexagon shapes and electronic states. Tunneling spectra taken on $Co_{0.8}Fe_{0.2}$ islands show an upward shift in the peak energy of the minority $d$ state as compared to pure Co islands. In the case of $Co_{0.5}Fe_{0.5}$, the peak energy is widely spread in the range of −0.2 to −0.4 eV within a single island. In the spin-polarized tunneling conductance maps, we observed spin contrasts on the islands with $x = 0$, 0.2, and 0.5. From the variation of the spin-sensitive signal with an external magnetic field, we found that the islands with $x = 0$, 0.2, and 0.5 exhibit the perpendicular magnetization.

## II. METHODS

The measurements were conducted with a low-temperature (6 K) ultra-high vacuum (UHV) STM (Unisoku USM-1300S paired with an RHK R9 controller). The magnetic field ($B_z$) perpendicular to the sample surface up to 2 T was achieved using a superconducting magnet. The Cu(111) single crystal was cleaned by repetitive cycles of $Ar^+$ sputtering and annealing (∼1000 K in a base pressure of $5 \times 10^{-8}$ Pa). The $Co_{1-x}Fe_x$/Cu(111) samples were prepared by co-deposition of Co and Fe on the clean Cu(111) surface, which was kept at room temperature during the deposition. There was no sign of hydrogen adsorption after 6.5 hours on the sample, which is situated in a liquid-He cooled UHV chamber (see Supplemental Material [44]). The $x$ values were determined by regulating the deposition rate of Co and Fe, which were calibrated by measuring the coverage of pure Co (Fe) islands on the Cu(111) surface from STM images ($R_{\text{Co}} = 3.63 \pm 0.03$ ML/min, $R_{\text{Fe}} = 3.64 \pm 0.02$ ML/min). The sources used for the deposition are Co and Fe rods from Alfa Aesar with the purity of 99.995%. The alloy compositions of $x = 0.2$, 0.5, and 0.8 are estimated as $0.20 \pm 0.03$, $0.50 \pm 0.03$, and $0.80 \pm 0.02$. For spin-averaged measurements, chemically etched W tips were used. The spin-polarized tips were prepared by high temperature (∼2000 K) flashing of the electrochemically etched W tips followed by Fe deposition. At zero magnetic field, the Fe-coated W tips prefer in-plane magnetization. The magnetized direction can, however, be rotated to the out-of-plane direction by the external magnetic fields [45]. A standard lock-in setup was used to record the differential tunneling conductance ($dI/dV$) spectra and maps with peak-to-peak bias voltage modulations ($V_{\text{mod}}^{\text{PP}}$) of 10, 20, or 50 mV at 971 Hz. All images were processed using Nanotech WSxM [46].

## III. RESULTS AND DISCUSSION

### A. Morphology of $Co_{1-x}Fe_x$ islands

STM images of $Co_{1-x}Fe_x$ with $x = 0$, 0.2, 0.5, 0.8 and 1 are presented in the upper panel of Figs. 1(a)–1(e), respectively. Most of the $Co_{1-x}Fe_x$ islands exhibit an identical height of around 0.4 nm, which indicates bilayer thickness of the islands. The morphology of the islands with $x = 0$ and 0.2 reveals triangular appearances, while the islands with $x = 0.5$ exhibit relatively irregular appearances. Hexagonal islands are found for $x = 0.8$ and 1. The corresponding differential tunneling conductance ($dI/dV$) maps of $Co_{1-x}Fe_x$ are displayed in the lower panel of Figs. 1(a)–1(e). The $dI/dV$ signals taken on pure Co islands [Fig. 1(a)] at the sample voltage of −300 mV, which corresponds to the vicinity of the Co $d_{3z^2-r^2}$ state, [25] show homogeneous intensity within an individual island. At the same voltage, the $dI/dV$ intensity varies within both $Co_{0.8}Fe_{0.2}$ and $Co_{0.5}Fe_{0.5}$ islands [Figs. 1(b) and 1(c)]. The nonuniform intensity distribution inside an individual island is due to the incorporation of Fe atoms, which could lead to local strain modification and/or redistribution of the charge density of the island. In the $dI/dV$ map of Fig. 1(d), the $Co_{0.2}Fe_{0.8}$ islands appear more defective than the pure Fe islands [Fig. 1(e)], which indicates the influence of Co atoms in Fe-rich islands.

### B. Electronic properties of $Co_{1-x}Fe_x$ islands

The tunneling spectra and STM images of Co-rich (Co and $Co_{0.8}Fe_{0.2}$) and Fe-rich (Fe and $Co_{0.2}Fe_{0.8}$) islands with similar sizes are displayed in Fig. 2. The locations at which

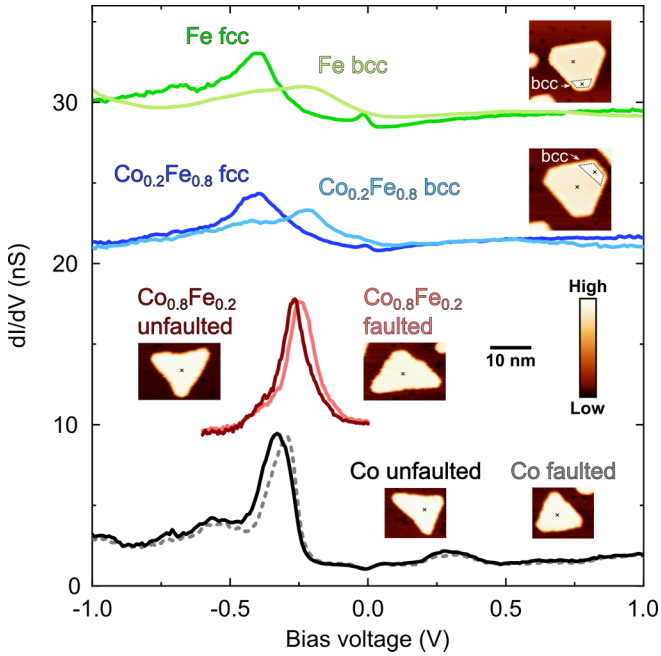


FIG. 2. Comparison of $dI/dV$ spectra taken on Co, $Co_{0.8}Fe_{0.2}$, $Co_{0.2}Fe_{0.8}$ and Fe islands. Inset STM images correspond to each island. The crosses mark the locations where the spectra were taken. The bcc areas are marked by dotted enclosures. STM images for unfaulted $Co_{0.8}Fe_{0.2}$: $V_s = -600$ mV, $I_t = 1$ nA; others: $V_s = -350$ mV, $I_t = 1$ nA. scale bar: 10 nm. Differential conductance spectra for $Co_{0.8}Fe_{0.2}$: $V_s = -600$ mV, $I_t = 1$ nA, $V_{\text{mod}}^{\text{PP}} = 20$ mV; others: $V_s = -350$ mV, $I_t = 1$ nA, $V_{\text{mod}}^{\text{PP}} = 20$ mV.

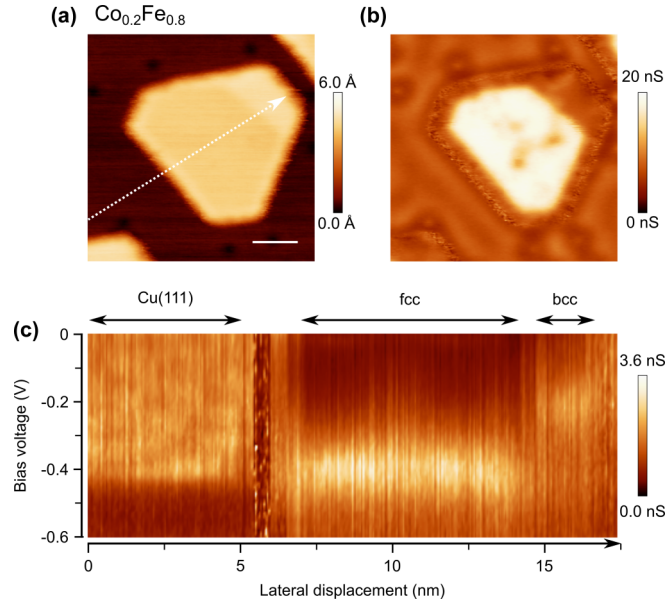


FIG. 3. (a) STM image and the corresponding $dI/dV$ image (b) of a $Co_{0.2}Fe_{0.8}$ island. The scale bars drawn in the STM image correspond to 4 nm. The white line indicates a route for taking the $dI/dV$ spectra. (c) Color-coded $dI/dV$ spectra arranged in the spatial sequence along the line in (a). Scanning parameters for [(a) and (b)]: $V_s = -350$ mV and $I_t = 1$ nA, and $V_{\text{mod}}^{\text{PP}} = 50$ mV. The spectra was taken with the stabilization condition of $V_s = 1$ V and $I_t = 1$ nA, and $V_{\text{mod}}^{\text{PP}} = 20$ mV.

the spectra were taken are marked by the crosses in the inset STM images. In the STM images of Co and $Co_{0.8}Fe_{0.2}$ islands [Figs. 1(a) and 1(b)], two types of triangular islands; one pointing upwards and the other pointing downwards, are found. The two correspond to either an island that has a stacking with the same crystallographic orientation as Cu(111) (unfaulted islands) or one whose $<11\bar{2}>$ direction is rotated by 180° (faulted islands) [47,48]. One way to distinguish the faulted and unfaulted islands is to compare the peak energy of the electronic states. For the islands with similar sizes, the faulted islands exhibit higher peak energy than the unfaulted islands. In Fig. 2, the dashed gray curve taken on the upward-pointing island (bottom-right inset STM image) shows a peak at −0.29 V, whereas the one (black curve) taken on the downward-pointing island (bottom-left inset STM image) shows a peak at −0.33 V. The upward-pointing islands are, therefore, assigned to faulted islands and the downward-pointing islands to unfaulted islands. We found that both unfaulted (dark red curve) and faulted (red curve) $Co_{0.8}Fe_{0.2}$ islands show higher peak energies than those of pure Co islands, suggesting hole doping by the Fe atom incorporation.

Within a single Fe island, domains with different tunneling spectra are found and attributed to the areas whose stacking is fcc (green curve) and bcc (light-green curve) [35]. The bcc-stacked area is often observed at the corner of the triangular islands. The stack-related domain structure was also observed in the $Co_{0.2}Fe_{0.8}$ islands. The spectra taken on center and corner sites of $Co_{0.2}Fe_{0.8}$ islands show similar features and identical peak energies to those of Fe islands, leading us to safely assign the fcc and bcc-stacking areas, respectively. The bcc areas are marked by dotted enclosures in the inset images of Fig. 2.

To further evidence the domain structure of fcc and bcc in the $Co_{0.2}Fe_{0.8}$ islands, we zoomed into a $Co_{0.2}Fe_{0.8}$ island and measured $dI/dV$ spectra continuously along a line (Fig. 3). Figure 3(a) displays an STM image of a $Co_{0.2}Fe_{0.8}$ island with a white line marking the positions where the tunneling spectra were taken. The corresponding $dI/dV$ map with the sample bias voltage of −0.3 V is shown in Fig. 3(b). We found a domain of low $dI/dV$ intensity at the upper right corner of the island, which exhibits elevated apparent height in the STM image [Fig. 3(a)]. The slightly high contrast in STM images is one of the characteristic features of the bcc-stacking area on a pure Fe island. The key difference between fcc and bcc areas is the peak energies, −0.22 V for fcc and −0.4 for bcc. In the color-coded $dI/dV$ spectra [Fig. 3(c)], we observed the two distinct peak energies and, therefore, assigned the corresponding areas to the fcc and the bcc-stacking area, respectively.

Due to the strain relaxation in Co nanoislands, their 3$d$ electronic states shift depending on their size [48]. In order to reveal the contribution of Fe atoms to the peak energy of the electronic states and thier shift, we measured size-dependent $dI/dV$ spectra on Co and $Co_{0.8}Fe_{0.2}$ islands (Fig. 4). Figures 4(a)–4(d) present the $dI/dV$ spectra of unfaulted Co, faulted Co, unfaulted $Co_{0.8}Fe_{0.2}$, and faulted $Co_{0.8}Fe_{0.2}$ islands, respectively. The corresponding sizes are written above the spectra. The island sizes are extracted from STM topographic images. We found that in all cases the peak bias

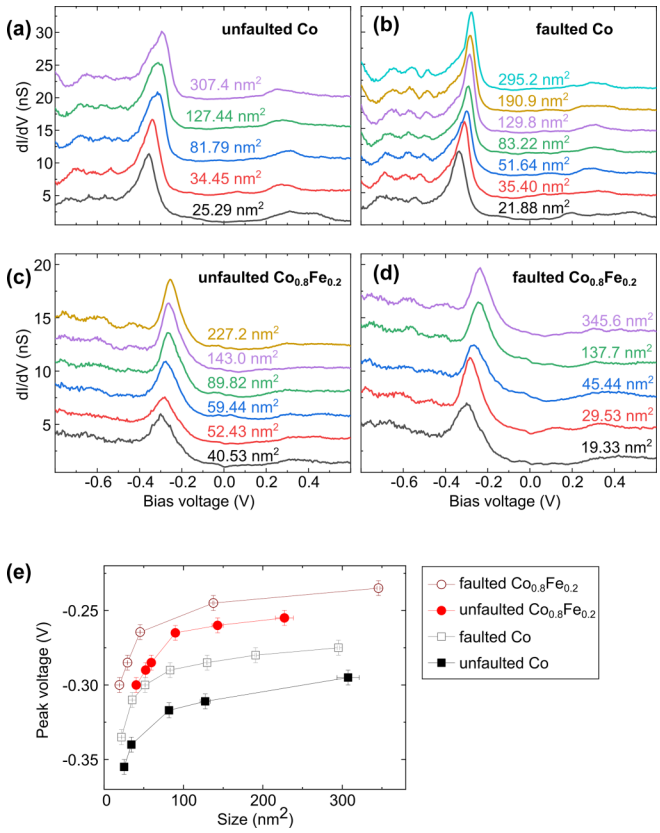


FIG. 4. Size-dependent $dI/dV$ spectra of (a) unfaulted Co islands, (b) faulted Co islands, (c) unfaulted $Co_{0.8}Fe_{0.2}$ islands, and (d) faulted $Co_{0.8}Fe_{0.2}$ islands. (e) Summary of the peak energies that extracted from [(a)–(d)] with respect to the island sizes. The spectra was taken with the stabilization condition of $V_s = -600$ mV and $I_t = 1$ nA, and $V_{\text{mod}}^{\text{PP}} = 10$ mV.

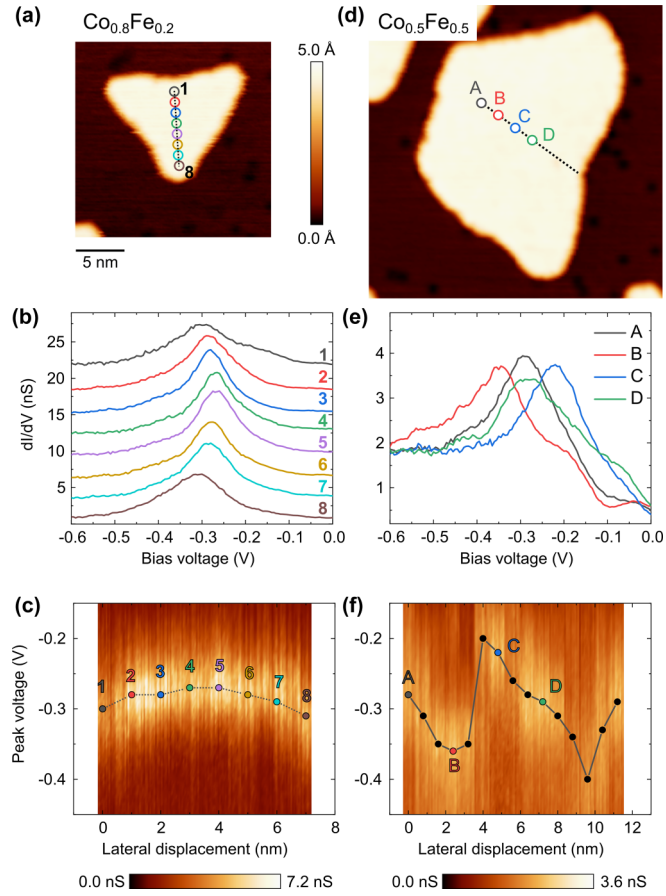


FIG. 5. (a) STM image of an unfaulted $Co_{0.8}Fe_{0.2}$ island. (b) Differential conductance ($dI/dV$) spectra taken at the positions marked as 1–8 in (a). Spectra are offset for clarity. (c) The corresponding peak energy extracted from (b). The background is color-coded $dI/dV$ spectra arranged in the spatial sequence along the line in (a). (d) STM image of a $Co_{0.5}Fe_{0.5}$ island. (e) Differential conductance spectra taken at the positions marked as A–D in (d). (f) Peak energy extracted from each spectrum taken along the profile in (d) including spectra A–D. Color-coded $dI/dV$ spectra taken along the line in (d) are underlaid. STM images [(a) and (d)]: $V_s = -600$ mV, $I_t = 1$ nA, scale bars: 5 nm. Differential conductance spectra [(b) and (e)]: $V_s = -600$ mV, $I_t = 1$ nA, $V_{\text{mod}}^{\text{PP}} = 20$ mV.

voltages (energies) exhibit upward shift with the island size. The peak energy as a function of the island size is plotted in Fig. 4(e). The unfaulted (faulted) $Co_{0.8}Fe_{0.2}$ islands show higher peak energy than unfaulted (faulted) Co islands regardless of their size. Accordingly, for both unfaulted and faulted $Co_{0.8}Fe_{0.2}$ islands, Fe atoms serve as a hole dopant to the electronic states. The peak variations of the electronic states with the island size originates from the strain induced by the lattice mismatch [48]. The lattice mismatch between the Co islands and the Cu(111) surface varies from 0.1% to 2% with decreasing the island size [48]. The crystallographic mismatch is most pronounced at the edge of the islands because of the reduced coordination there. In fact, for small islands, their properties are dominated by the edges, which emphasize the lattice mismatch with the substrate. In the case of Fe/Cu(111), the macroscopic lattice mismatch is 0.8% for fcc Fe(111) as reported in Ref. [49], which is comparably small. Accordingly, when mixing Co with Fe, the lattice mismatch of the alloy nanomagnets is presumably modified from the pure ones.

In order to obtain more information about the spatial distribution of the $dI/dV$ intensity, we measured $dI/dV$ spectra across islands of $Co_{0.8}Fe_{0.2}$ and $Co_{0.5}Fe_{0.5}$. Figure 5(a) presents an STM image of a $Co_{0.8}Fe_{0.2}$ island. The locations where the tunneling spectra are taken are marked by colored circles numbered from 1 to 8. The $dI/dV$ spectra at the locations of 1 to 8 are displayed in Fig. 5(b). Each spectrum reveals a pronounced peak at around −0.3 V. The peak energies are extracted and summarized in Fig. 5(c) overlaid with a color-coded $dI/dV$ spectra taken along the dotted line in Fig. 5(a). A continuous change in the peak energy with respect to the location is found. The peak energy shifts toward lower energy near the edges of the island, i.e., in the spectra numbered 1 and 8. A similar phenomenon has been reported for pure Co islands and attributed to the reduced strain near the edge. [48] At the center (locations 4 and 5) of the island, the state is found with a peak at −0.27 V. Comparing to the peak energy (−0.33 V) of the pure Co islands with a similar size, the Fermi level of $Co_{0.8}Fe_{0.2}$ islands shifted down by around 60 mV. Such downward shift of the Fermi level indicates hole doping into the islands.

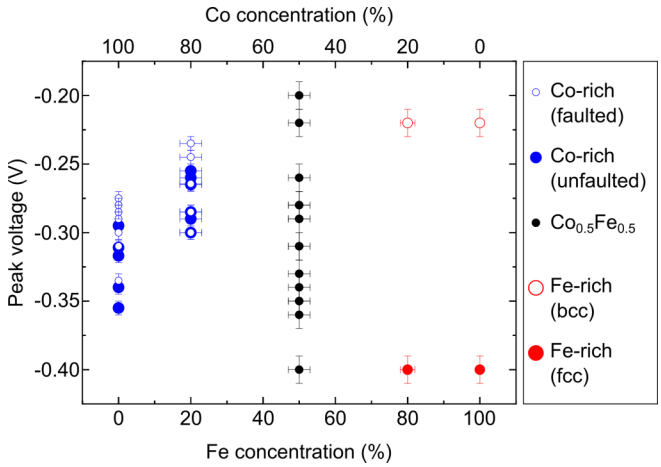


FIG. 6. Summary of the surface state peak postion with respect to different $Co_{1-x}Fe_x$ compositions.

Figure 5(d) shows a typical STM image of a $Co_{0.5}Fe_{0.5}$ island. Tunneling conductance spectra taken at designated locations (marked as A–D) along the dotted line are presented in Fig. 5(e). The peak energy is found to be strongly dependent on the measured locations. Figure 5(f) summarizes the peak energies along the line, which spans 11.5 nm. The peak energies are distributed in the range of $-0.2$ to $-0.4$ V. Such distribution is also visualized in the color-coded $dI/dV$ spectra taken along the line [background of Fig. 5(f)]. The spatial variation of the peak energy [Fig. 5(f)] is significantly larger than the case in pure Co [48] and $Co_{0.8}Fe_{0.2}$ [Fig. 5(c)]. The peak variation has two possible origins: hole doping effects and strain relaxations. The doping by the introduction of Fe atoms is expected to be independent of the location since electrons will redistribute within the metallic island. The strain relaxation, on the other hand, gives rise to the peak energy difference, as shown in the spectra taken at the center and the edge of the island. In addition, the spatial peak energy variations could be due to structural variations, e.g., local fcc and bcc distribution within the island, which could be induced during the process of the strain relaxation. Increasing the amount of Fe to 50% makes the island appearances [Fig. 1(c)] different from the pure Co island [Fig. 1(a)]. Therefore, the observed spatial-dependent peak energies in $Co_{0.5}Fe_{0.5}$ islands are presumably due to the inhomogeneous strain distribution and/or the local structural variations by the introduction of Fe.

The peak energies on the islands are summarized in Fig. 6. The blue circles represent the peak energies extracted from Figs. 4(a)–4(d) of pure Co and $Co_{0.8}Fe_{0.2}$ islands (open circle: faulted islands; solid circle: unfaulted islands). For $Co_{0.5}Fe_{0.5}$, the peak energies are extracted from Fig. 5(f) and presented as black circles. The peak energies of Fe and $Co_{0.2}Fe_{0.8}$ islands are extracted from Fig. 2 and marked with red circles (open circle: bcc; solid circle: fcc). In the Co-rich regime, peak shift due to the doping effect was observed. In the case when the ratio between Co and Fe is 1:1, the peak energies are distributed in the range from $-0.2$ to $-0.4$ V depending on the location. In the Fe-rich regime, no pronounced peak energy differences are observed. The possible reason for no-shift in the Fe-rich regime could be a certain degree of intermixing between Co and Cu during the growth [28,50,51], which diminishes the doping effect by Co.

### C. Magnetic properties of $Co_{1-x}Fe_x$ islands

Spin-polarized imaging is achieved using Fe-coated W-tips, which have easy-plane anisotropy [52,53]. The out-of-plane magnetization component of the tip can be regulated by the application of out-of-plane magnetic field ($B_z$). Figure 7(a) schematically illustrates the magnetization direction of the tip with respect to the sample surface. With the presence of $B_z$, the magnetization of the tip is canted toward the out-of-plane directions, which reveals the out-of-plane spin contrast of the $Co_{1-x}Fe_x$ islands ($x = 0$, 0.2, 0.5). The z-component of the tip magnetization ($M_z^{\mathrm{tip}}$) behaves in a paramagnetic manner with $B_z$.

Figure 7(b) shows the $dI/dV$ maps of pure Co islands on Cu(111). The bias voltage was set at $-300$ mV to probe the spin-polarized electronic states. At $B_z = 0.2$ T, a contrast was observed between the Co islands, which corresponds to the difference in the spin-polarized tunneling conductance between the up and down magnetized Co islands. At zero field, all islands show the same $dI/dV$ intensity, which implies orthogonal configuration between the tip and sample magnetizations. When measuring at the opposite fields ($B_z = -0.2$ T), some islands show reversed contrast while the others remain identical compared with the map at 0.2 T. Since the $z$ component of the tip magnetization ($M_z^{\mathrm{tip}}$) changes its direction, the observed contrast reversal indicates persistent perpendicular magnetization of the islands in the range of the applied magnetic fields. The islands with the identical intensity indicate that their magnetizations switch during the magnetic-field flip from 0.2 to $-0.2$ T. Since the anisotropic energy is proportional to the island size, smaller islands tend to flip at lower magnetic fields than larger ones [29,30], consistent with the trend observed in our spin-polarized maps.

Figure 7(c) displays the spin-polarized $dI/dV$ maps of $Co_{0.8}Fe_{0.2}$ islands ($V_s = -500$ mV) measured under different magnetic fields of 0.08, 0, and $-0.08$ T from the top to the bottom panel. Pronounced spin contrast inversion is observed on large islands, which indicates the persistent existence of the perpendicular magnetization. In the case of $Co_{0.5}Fe_{0.5}$ [Fig. 7(c)], we found most of the islands exhibit spin contrast inversion when switching from 0.2 to $-0.2$ T, even for smaller islands. The observed spin contrast inversion confirms the persistent perpendicular magnetization of $Co_{0.5}Fe_{0.5}$ islands with larger anisotropy than pure Co islands.

The alloyed islands favor perpendicular magnetization at $x = 0.2$ and 0.5. In the case of Fe-rich islands ($x = 0.8$, 1), $Co_{0.2}Fe_{0.8}$ islands exhibit similar topographic appearance and spectra to the pure Fe islands. The magnetic properties of Fe islands have been reported that the fcc phase of Fe on Cu(111) shows layer-wise antiferromagnetic configuration [35], while the bcc Fe prefers ferromagnetic with perpendicular anisotropy [54]. Obviously the anisotropy of the $Co_{1-x}Fe_x$ islands is expected to vary depending on the ratio. To investigate the variation in the anisotropy requires hysteresis measurements. Our work presented here would be a starting point for these future experiments.

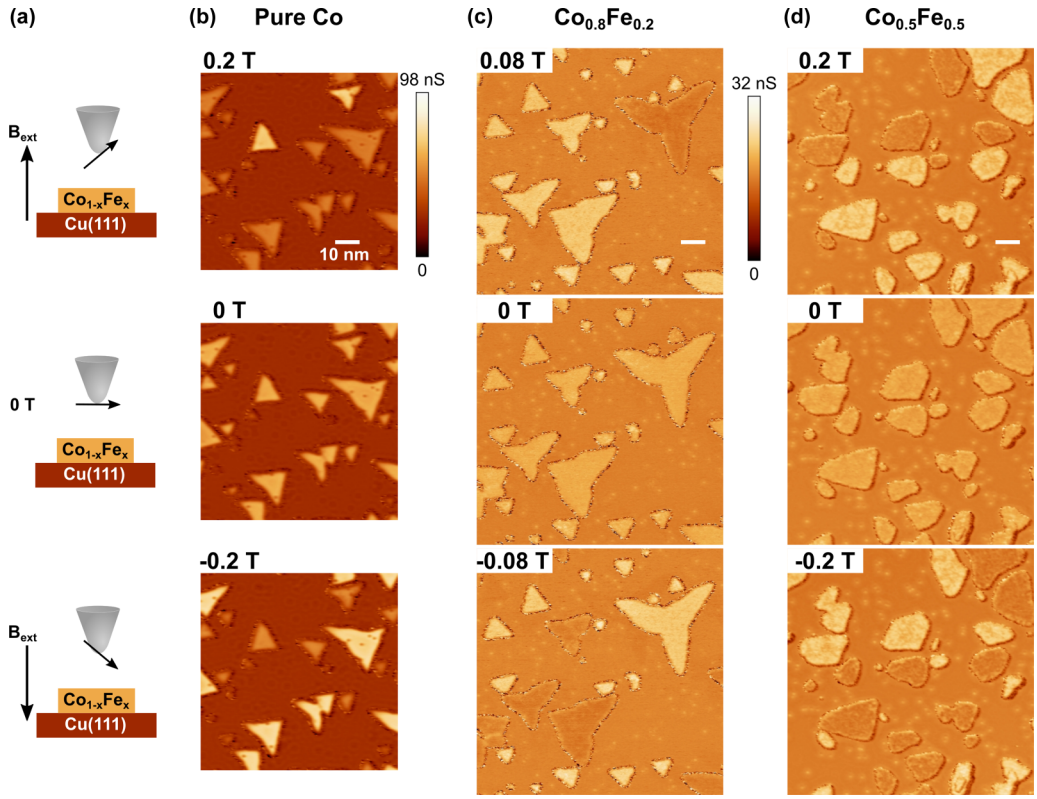


FIG. 7. (a) Schematics of the magnetization of the Fe-coated W tip under external fields. Fe-coated W tips exhibit in-plane easy axis and paramagnetic-like hysteresis along out-of-plane direction. (b) Spin-polarized tunneling conductance maps of pure Co islands on Cu(111) at 0.2 T (top), 0 T (middle), and −0.2 T (bottom). (c) Spin-polarized tunneling conductance maps of $Co_{0.8}Fe_{0.2}$ islands on Cu(111) at 0.08 T (top), 0 T (middle), and −0.08 T (bottom). (d) Spin-polarized tunneling conductance maps of $Co_{0.5}Fe_{0.5}$ islands on Cu(111) at 0.2 T (top), 0 T (middle), and −0.2 T (bottom). Imaging conditions (b) $V_s = -300$ mV, $I_t = 1$ nA, $V_{\text{mod}}^{\text{PP}} = 50$ mV. [(c) and (d)] $V_s = -500$ mV, $I_t = 1$ nA, $V_{\text{mod}}^{\text{PP}} = 50$ mV.

## IV. CONCLUSION

By codeposition of Co and Fe, nanomagnets of $Co_{1-x}Fe_x$ on Cu(111) with the alloy composition of $x = 0$, 0.2, 0.5, 0.8, and 1 were prepared. Using spin-averaged STM, we found similar appearances between islands with $x = 0$ and 0.2. Tunneling conductance spectra taken on islands with $x = 0.2$ show an upward-shifted peak as compared to those of $x = 0$, indicating hole doping due to the Fe incorporation. On the other hand, for $x = 0.5$, round-shaped nanomagnets are formed instead of triangular ones as it is the case for $x = 0$ and 0.2. In addition, the peak energy irregularly distributes in the range between −0.2 to −0.4 V within a single nanomagnet. The spatially dependent peak energies suggest a local strain distribution and/or structural variations. For islands with $x = 0.8$ and 1, the islands exhibit similar hexagonal shape and electronic states with the same peak energies. The perpendicular magnetization of the $Co_{1-x}Fe_x$ nanomagnets with $x = 0$, 0.2, and 0.5 is identified using spin-polarized STM. We found that the perpendicular magnetization of the $Co_{1-x}Fe_x$ nanomagnets is robust against alloying with Fe at least up to 50%.

## ACKNOWLEDGMENTS

This work is partially supported by Grants-in-Aid for Scientic Research from the Japan Society for the Promotion of Science (Grants No. JP16H02109, No. JP18K19013, and No. JP19H00859) and Ministry of Science and Technology of Taiwan under Grant No. MOST 108-2112-M-003-011-MY2.

[1] M.-T. Lin, J. Shen, W. Kuch, H. Jenniches, M. Klaua, C. M. Schneider, and J. Kirschner, Phys. Rev. B **55**, 5886 (1997).

[2] S. Müller, P. Bayer, C. Reischl, K. Heinz, B. Feldmann, H. Zillgen, and M. Wuttig, Phys. Rev. Lett. **74**, 765 (1995).

[3] D. P. Pappas, C. R. Brundle, and H. Hopster, Phys. Rev. B **45**, 8169 (1992).

[4] J. A. Bland, G. A. Gehring, B. Kaplan, and C. Daboo, J. Magn. Magn. Mater. **113**, 173 (1992).

[5] J. Thomassen, F. May, B. Feldmann, M. Wuttig, and H. Ibach, Phys. Rev. Lett. **69**, 3831 (1992).

[6] W. Platow, U. Bovensiepen, P. Poulopoulos, M. Farle, K. Baberschke, L. Hammer, S. Walter, S. Müller, and K. Heinz, Phys. Rev. B **59**, 12641 (1999).

[7] K. Ha, M. Ciria, R. C. O'Handley, P. W. Stephens, and P. Pagola, Phys. Rev. B **60**, 13780 (1999).

[8] D. P. Pappas, K. P. Kämper, and H. Hopster, Phys. Rev. Lett. **64**, 3179 (1990).

[9] P. Krams, F. Lauks, R. L. Stamps, B. Hillebrands, G. Güntherodt, and H. P. Oepen, J. Magn. Magn. Mater. **121**, 483 (1993).

[10] M. Kowalewski, C. M. Schneider, and B. Heinrich, Phys. Rev. B **47**, 8748 (1993).

[11] M.-T. Lin, J. Shen, J. Giergiel, W. Kuch, H. Jenniches, M. Klaua, C. M. Schneider, and J. Kirschner, Thin Solid Films **275**, 99 (1996).

[12] W. L. O'Brien and B. P. Tonner, Phys. Rev. B **49**, 15370 (1994).

[13] G. Bochi, C. A. Ballentine, H. E. Inglefield, C. V. Thompson, R. C. O'Handley, H. J. Hug, B. Stiefel, A. Moser, and H.-J. Guntherodt, Phys. Rev. B **52**, 7311 (1995).

[14] S. Z. Wu, G. J. Mankey, F. Huang, and R. F. Willis, J. Appl. Phys. **76**, 6434 (1994).

[15] F. Huang, M. T. Kief, G. J. Mankey, and R. F. Willis, Phys. Rev. B **49**, 3962 (1994).

[16] B. Schulz and K. Baberschke, Phys. Rev. B **50**, 13467 (1994).

[17] Y. Shiratsuchi, M. Yamamoto, and S. D. Bader, Prog. Surf. Sci. **82**, 121 (2007).

[18] A. Williams, V. Moruzzi, A. Malozemoff, and K. Terakura, IEEE Trans. Magn. **Mag-19**, 1983 (1983).

[19] H. T. Jeng and D. S. Wang, J. Magn. Magn. Mater. **317**, 46 (2007).

[20] A. Dittschar, M. Zharnikov, W. Kuch, M.-T. Lin, C. M. Schneider, and J. Kirschner, Phys. Rev. B **57**, R3209 (1998).

[21] M.-T. Lin, W.-C. Lin, C.-C. Kuo, and C.-L. Chiu, Phys. Rev. B **62**, 14268 (2000).

[22] C.-C. Kuo, S.-F. Chuang, W. Pan, W.-C. Lin, and M.-T. Lin, J. Appl. Phys. **91**, 7185 (2002).

[23] H. Oka, P. A. Ignatiev, S. Wedekind, G. Rodary, L. Niebergall, V. S. Stepanyuk, D. Sander, and J. Kirschner, Science **327**, 843 (2010).

[24] K. Edelmann, L. Wilmes, V. Rai, L. Gerhard, L. Yang, M. Wegener, T. Repän, C. Rockstuhl, and W. Wulfhekel, Phys. Rev. B **101**, 205405 (2020).

[25] L. Diekhöner, M. A. Schneider, A. N. Baranov, V. S. Stepanyuk, P. Bruno, and K. Kern, Phys. Rev. Lett. **90**, 236801 (2003).

[26] J. Park, C. Park, M. Yoon, and A. P. Li, Nano Lett. **17**, 292 (2017).

[27] M. Corbetta, S. Ouazi, J. Borme, Y. Nahas, F. Donati, H. Oka, S. Wedekind, D. Sander, and J. Kirschner, Jpn. J. Appl. Phys. **51**, 5 (2012).

[28] O. Pietzsch, A. Kubetzka, M. Bode, and R. Wiesendanger, Phys. Rev. Lett. **92**, 057202 (2004).

[29] S. Wedekind, G. Rodary, J. Borme, S. Ouazi, Y. Nahas, M. Corbetta, H. Oka, D. Sander, and J. Kirschner, IEEE Trans. Magn. **47**, 3351 (2011).

[30] S. Ouazi, S. Wedekind, G. Rodary, H. Oka, D. Sander, and J. Kirschner, Phys. Rev. Lett. **108**, 107206 (2012).

[31] J. Shen, R. Skomski, M. Klaua, H. Jenniches, S. S. Manoharan, and J. Kirschner, Phys. Rev. B **56**, 2340 (1997).

[32] A. Biedermann, W. Rupp, M. Schmid, and P. Varga, Phys. Rev. B **73**, 165418 (2006).

[33] C. Boeglin, S. Stanescu, J. P. Deville, P. Ohresser, and N. B. Brookes, Phys. Rev. B **66**, 014439 (2002).

[34] J. P. Pierce, M. A. Torija, Z. Gai, J. Shi, T. C. Schulthess, G. A. Farnan, J. F. Wendelken, E. W. Plummer, and J. Shen, Phys. Rev. Lett. **92**, 237201 (2004).

[35] L. Gerhard, T. K. Yamada, T. Balashov, A. F. Takács, R. J. H. Wesselink, M. Däne, M. Fechner, S. Ostanin, A. Ernst, I. Mertig, and W. Wulfhekel, Nat. Nanotechnol. **5**, 792 (2010).

[36] S. Shiraki, H. Fujisawa, T. Nakamura, T. Muro, M. Nantoh, and M. Kawai, Phys. Rev. B **78**, 115428 (2008).

[37] W.-C. Lin, H.-Y. Chang, Y.-C. Hu, and C.-C. Kuo, IEEE Trans. Magn. **45**, 4037 (2009).

[38] F. Donati, A. Mairov, C. S. Casari, M. Passoni, and A. Li Bassi, Surf. Sci. **606**, 702 (2012).

[39] A. Delga, J. Lagoute, V. Repain, C. Chacon, Y. Girard, M. Marathe, S. Narasimhan, and S. Rousset, Phys. Rev. B **84**, 035416 (2011).

[40] K. Doi, E. Minamitani, S. Yamamoto, R. Arafune, Y. Yoshida, S. Watanabe, and Y. Hasegawa, Phys. Rev. B **92**, 064421 (2015).

[41] V. Repain, J. M. Berroir, S. Rousset, and J. Lecoeur, Surf. Sci. **447**, L152 (2000).

[42] P. Mishra, Z. K. Qi, H. Oka, K. Nakamura, and T. Komeda, Nano Lett. **17**, 5843 (2017).

[43] C. Didiot, A. Tejeda, Y. Fagot-Revurat, V. Repain, B. Kierren, S. Rousset, and D. Malterre, Phys. Rev. B **76**, 081404(R) (2007).

[44] See Supplemental Material at http://link.aps.org/supplemental/10.1103/PhysRevB.104.035422 for the STM images and the corresponding dI/dV images on a pure Co island with a time separation of 6.5 hours.

[45] M. Haze, Y. Yoshida, and Y. Hasegawa, Phys. Rev. B **95**, 060415(R) (2017).

[46] I. Horcas, R. Fernández, J. M. Gómez-Rodríguez, J. Colchero, J. Gómez-Herrero, and A. M. Baro, Rev. Sci. Instrum. **78**, 13705 (2007).

[47] A. L. Vázquez de Parga, F. J. García-Vidal, and R. Miranda, Phys. Rev. Lett. **85**, 4365 (2000).

[48] M. V. Rastei, B. Heinrich, L. Limot, P. A. Ignatiev, V. S. Stepanyuk, P. Bruno, and J. P. Bucher, Phys. Rev. Lett. **99**, 246102 (2007).

[49] M. T. Kief and W. F. Egelhoff, Phys. Rev. B **47**, 10785 (1993).

[50] J. Khalil, G. Bozzolo, D. Farías, A. L. Vázquez de Parga, J. J. de Miguel, and R. Miranda, MRS Online Proceedings Library **696**, 93 (2001).

[51] A. Rabe, N. Memmel, A. Steltenpohl, and T. Fauster, Phys. Rev. Lett. **73**, 2728 (1994).

[52] S. Meckler, N. Mikuszeit, A. Preßler, E. Y. Vedmedenko, O. Pietzsch, and R. Wiesendanger, Phys. Rev. Lett. **103**, 157201 (2009).

[53] S.-h. Phark, J. A. Fischer, M. Corbetta, D. Sander, and J. Kirschner, Appl. Phys. Lett. **103**, 032407 (2013).

[54] S. H. Phark, J. A. Fischer, M. Corbetta, D. Sander, K. Nakamura, and J. Kirschner, Nat. Commun. **5**, 5183 (2014).